

Optimizing the Surface Characteristics of $\text{La}_{0.6}\text{Sr}_{0.4}\text{CoO}_{3-\delta}$ Perovskite Oxide by Rapid Flash Sintering Technology for Easy Fabrication and Fast Reaction Kinetics in Alkaline Medium

Maria Christy, Hashikaa Rajan, Hwichul Yang, and Young-Beom Kim*



Cite This: *Energy Fuels* 2020, 34, 16838–16846



Read Online

ACCESS |

Metrics & More

Article Recommendations

Supporting Information

ABSTRACT: Perovskites are a challenging new class of highly efficient bifunctional catalysts that hold huge significance in advanced batteries and water electrolysis. The surface chemistry and surface electronic structures of the $\text{La}_{0.6}\text{Sr}_{0.4}\text{CoO}_{3-\delta}$ (LSC) perovskite is greatly modified upon postsynthesis sintering. Herein, a new strategy has been demonstrated by intense pulsed light technology to accomplish the sintering process in milliseconds, and is comparatively explored with conventionally sintered LSC. The optimized sintering conditions rejuvenated a new class of a highly active bifunctional LSC electrocatalyst. The electrochemical activity and surface characteristics are orders of magnitude superior to those of the thermally sintered LSC. The best performing LSC catalyst known as LSC 30 exhibits outstanding bifunctionality with a low overpotential (~ 0.89 V). Furthermore, LSC 30 shows a positively shifted onset potential of 0.92 V and a high limiting current of -6.1 mA cm^{-2} at 20 mV s^{-1} , during the oxygen reduction reaction in alkaline medium. When tested as the air cathode of a zinc–air battery, LSC 30 delivered a steady performance for 200 cycles. This study highlights the role of the new concept in the agile synthesis of perovskite oxides for oxygen catalysis and possible application as the air cathode in metal air batteries.

INTRODUCTION

In the pursuit of sustainable energy, it is critical to produce cost-effective as well as highly active electrocatalysts. Perovskite oxides have been investigated as catalysts for a large variety of reactions where perovskites with a general formula ABO_3 hold great assurance to be efficient bifunctional catalysts.^{1–5} The desirability of perovskite oxides is the flexibility of tuning their physical, chemical, and catalytic properties. Particularly, the $\text{La}_{0.6}\text{Sr}_{0.4}\text{CoO}_{3-\delta}$ (LSC) perovskite is a classic bifunctional catalyst used for oxygen reduction and evolution reactions (ORR and OER) in fuel cells and metal–air batteries.^{6–10} These oxides are highly stable at elevated temperatures and possess a high electronic/ionic conductivity, which makes them promising electrocatalysts. In that aspect, the optimization of perovskite oxides to advance their catalytic phenomenon has been drastically increased in the past few decades. However, synthesis of LSC is still a complicated process, which involves high temperature that could possibly generate impurities. Out of the assorted synthetic techniques like mechanical synthesis, coprecipitation, and so forth, the Pechini method is highly favored because, in this method, various metal ions chelate to form metal complexes in solution that are uniformly distributed at the molecular level.¹¹ The synthesized material is then sintered to obtain a phase-pure high-quality material with improved electrical conductivity. It has been confirmed that the LSC oxides sintered at higher temperatures (1000 °C or above) exhibit a stable perovskite structure without the SrCO_3 impurity phase. Moreover, the high-temperature-sintered LSC seems to exhibit superior electrocatalytic activity compared to the as-synthesized, nonsintered material.^{8,12–16}

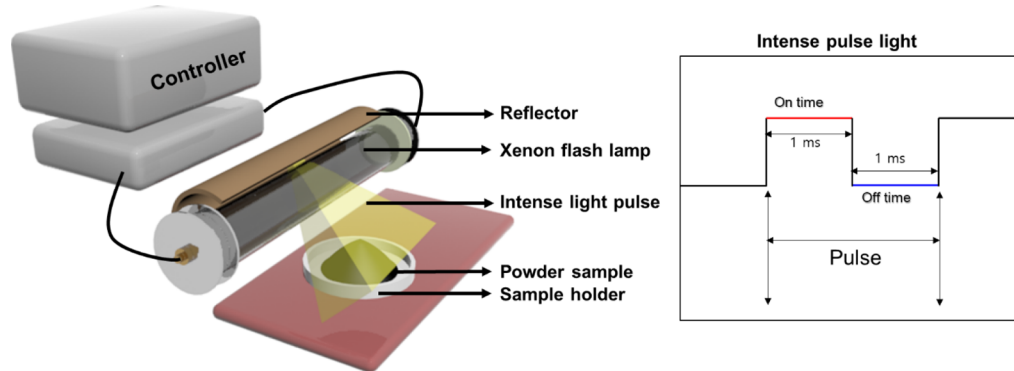
Recently, intense pulsed-light (IPL) sintering has emerged as an ideal method with the advantages of high speed, efficiency, and the ability to perform at room temperature. IPL technology basically applies pulsed visible broad-spectrum (350–750 nm) light from a xenon lamp to sinter nanoparticles into films used in functional devices. Compared to conventional oven-based sintering methods or other rapid thermal, laser, microwave and electrical methods, the IPL process has specific advantages of covering a large surface area and a high speed. Thermal annealing methods require direct conduction or convection processes that require a high temperature. Furthermore, the dwell time usually ranges from minutes to hours to days that includes heating ramp and cooling time. By replacing IPL, the sintering process is accomplished in milliseconds just by irradiating the material with high energy density flashes that favorably result in highly catalytic oxides. Though highly meritorious for easy fabrication of various materials, IPL has been scarcely utilized in the field of catalysis. Intrigued by these fortunate developments, in this work, we seek the simplest, easiest, and fastest sintering of LSC that will attain the aforesaid correlation between phase-purity and intrinsic catalytic activity of the material. Though IPL technology has been established as an extremely efficient method to produce high-performance nanomaterial-based

Received: September 18, 2020

Revised: October 31, 2020

Published: November 25, 2020



Scheme 1. Schematic Representation of Intense Pulse Light Sintering

electrodes, most of the studies involve thin films.^{17–21} In this work, a facile sintering of LSC powders by IPL technology is proposed that is agile, effective, and scalable.

In detail, the LSC catalyst material is synthesized using the Pechini method and irradiated by IPL for sintering. IPL is performed for various energy densities by adjusting the irradiation energy, time, pulse duration, and pulse quantity (refer Table S1 from Supporting Information and Scheme 1). Depending on the IPL energy used viz. 10, 30, and 50 J cm⁻², the IPL-treated LSCs are named as LSC 10, LSC 30, and LSC 50, respectively. For comparison, a batch of freshly prepared LSC is also conventionally sintered at 1000 °C in air, referred to as LSC A. All the prepared LSC catalysts are analyzed for electrocatalytic performances namely ORR and OER in alkaline 0.1 M KOH medium. The IPL sintering aids in the easy and fast synthesis of the material, and in addition, the electrocatalytic activity of IPL-treated LSC supersedes the overall performance of conventional LSC A with better reaction kinetics. Among them, LSC 30 exhibits superior bifunctional catalytic activity with lowest obtained over potential of ~0.89 V, and, a positively shifted onset potential of 0.92 V and a high limiting current of -6.1 mA cm^{-2} at 20 mV s⁻¹ for ORR. The best performing LSC 30, when applied in a zinc–air battery as an air cathode, delivered a steady performance for 200 cycles.

EXPERIMENTAL SECTION

Material Synthesis of LSC. The perovskite LSC was synthesized using the Pechini method.¹¹ The chemicals, La(NO₃)₃·6H₂O (99.9%, Sigma-Aldrich), Sr(NO₃)₂ (99%, Sigma-Aldrich), and Co(NO₃)₂·6H₂O (97.7%, Sigma-Aldrich) were purchased and used without further purification. The precursor materials [La(NO₃)₃·6H₂O: 7.801 g, Sr(NO₃)₂: 2.565 g, and Co(NO₃)₂·6H₂O: 8.936 g] in a stoichiometric ratio of (0.6:0.4:1) were dissolved in 30 mL deionized water and 1 M mixed solution was prepared. 2 M aqueous citric acid solution was prepared and added into the mixed solution to form a metal complex compound. Ethylene glycol (99%, Sigma-Aldrich) was added as a cross-linking agent and the solution was continuously stirred for 2 h at 80 °C. At this point, gel-like consistency was obtained because of the formation of poly resin. Thus formed gel was dried at a constant temperature of 80 °C and the resulting polymer resin was carbonized for 1 h at 400 °C to remove any residues. Finally, the solid products were collected and ground in a crucible to obtain LSC powders. A small amount of LSC was sintered at 1000 °C to obtain phase pure material without any impurity and referred to as LSC A. The rest of the as-prepared LSC were treated with IPL technology.

IPL Sintering. The IPL sintering was carried out in myPET-LM200 by Semisysco and the applied flash light energy (energy density: 10–50 J cm⁻²) was measured using a power meter (Nova II,

People Laser Tech Inc., South Korea). The typical flashlight sintering system consists of a xenon lamp with a power supply, pulse controller, reflector, and a computer-controlled system, as illustrated in Scheme 1. The wavelength of the emitted light ranges from 380 to 750 nm. The flashlight sintering process was controlled by its energy (J cm⁻¹) per pulse, time of exposure (seconds), duration of pulse (seconds), and number of pulses (#). In this case, the powder samples were evenly distributed in a quartz glass Petri dish (65 × 10 mm size) with a lid, at a distance of ~1 to 1.5 cm from the light source for IPL sintering. In order to follow the results clearly and to understand the post-treatment properties, a range of energy was chosen. The irradiation energy was varied from 10 to 30 and 50 J cm⁻¹ to assure lower to higher order and post-IPL sintered samples are known as LSC 10, LSC 30, and LSC 50, respectively. The irradiation energy is detailed in Table S1 (Supporting Information).

Material Characterization. The phase identification of the prepared LSC catalysts was examined using an X-ray diffractometer (XRD) (D8 ADVANCE, Bruker Co.). The morphology, particle size, and crystallographic information of the samples was characterized by field emission-scanning electron microscopy (FE-SEM, Hitachi, S-4800) and high-resolution transmission electron microscopy (HR-TEM, JEM-2100F). X-ray photo electron spectroscopy (XPS) analysis (PHI 5000 VersaProbe, ULVAC-PHI, Japan) was utilized to analyze the chemical states. Brunauer–Emmett–Teller (BET) technique was used to find the specific surface area, pore size, and pore volume of the synthesized LSC materials.

Electrochemical Characterization. Electrocatalytic activity of the sample was evaluated by measuring ORR and OER polarization curves using cyclic voltammetry (CV) and linear sweep voltammetry (LSV) techniques in a three-electrode electrochemical cell with a rotating disk electrode (RDE) (AFMSRCE, Pine Instrumentation) and a potentiostat/galvanostat workstation (Gamry Reference 3000). To prepare the working electrode, the catalyst ink was prepared by mixing the catalyst (3 mg) and carbon powders (7 mg, Cabot VULCAN XC-72). The mixture was dispersed ultrasonically in 150 μL of diluted 5 wt % Nafion alcohol solution and about 10 μL of the suspension was pipetted onto a glassy carbon substrate. A Pt wire and Hg/HgO were used as the counter and reference electrodes, respectively. 0.1 M KOH aqueous solution was employed as the electrolyte. The half-cell with the KOH electrolyte was purged with oxygen flow for an hour to saturate the electrolyte with oxygen. The CV measurements were performed at a scan rate of 20 mV s⁻¹ in a potential window of −0.8 to 0.3 V. To measure the ORR and OER polarization curves, the LSV was recorded in a potential window of −0.8 to 0.2 and 0.2 to 1.0 V, respectively, at a scan rate of 20 mV s⁻¹ and a varying disk rotation speed ranging from 400 to 2400 rpm.

Zinc–Air Battery Fabrication. A zinc–air battery in a homemade cell setup was fabricated with a Zn film of 0.25 mm thickness as the anode and 1 mg·cm⁻² catalyst ink-coated gas diffusion layer (GDL) as the air cathode in an aqueous 0.2 M zinc acetate in 6 M KOH electrolyte. For the preparation of cathode ink, 15 mg of the as-prepared active material with 100 μL of 5 wt % Nafion solution was dispersed in 1.5 mL of isopropyl alcohol by sonication for 30 min.

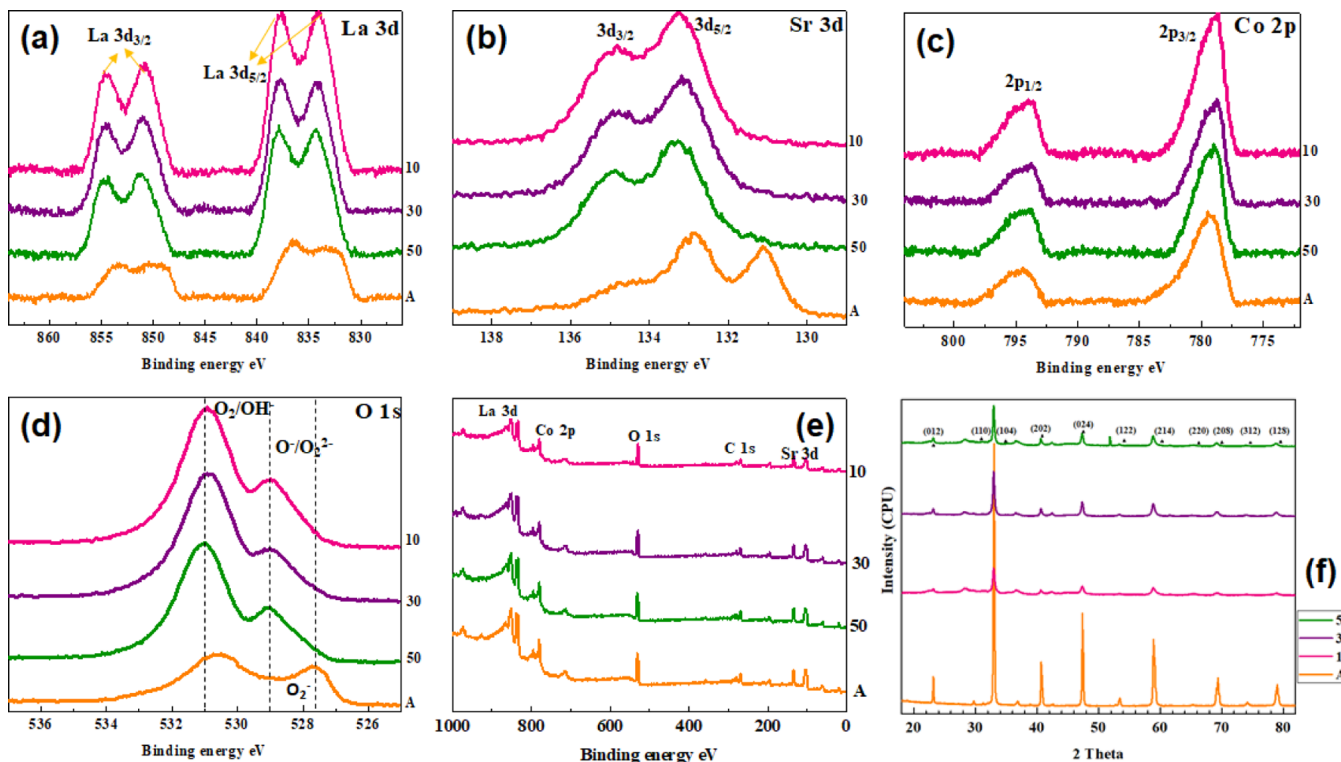


Figure 1. XPS analysis of (a) La 3d (b) Sr 3d, (c) Co 2p and (d) O 1s peaks, (e) XPS survey, and (f) XRD pattern of LSC perovskites.

The catalyst mixture was sprayed onto the GDL in an eS robot spray coater and vacuum dried at 60 °C. The catalyst loading was determined by measuring the weight of the GDL before and after coating. The charge–discharge pulse cycling was conducted by a recurrent galvanic pulse method with a fixed current of 5 mA cm⁻² with each cycle being 10 min (5 min discharge followed by 5 min charge) and tested sufficiently for consistency.

RESULTS AND DISCUSSION

Material Characterization. LSC catalysts are prepared using the superfast IPL technology and the various physical characterizations were carried out to understand the materials in detail. The chemical composition and oxidation states of the elements are analyzed by XPS as shown in Figure 1a–e. The high-resolution deconvolution peaks of La 3d with binding energies of 833.6 and 837.2 eV can be assigned to La 3d_{5/2} and La 3d_{3/2}, respectively, Figure 1a. The small variations of the La 3d_{5/2} peak's binding energy at 833.6 and the spin–orbit splitting (~16.92 eV) affirm the La³⁺ ions near the oxygen deficient sites. The Sr 3d peak is positioned at (131.3 ± 0.2 and 133 ± 0.2 eV) for 3d_{5/2} and (134.3 ± 0.2 eV) for 3d_{3/2} (Figure 1b). The lower and higher energy peaks arise from the perovskite crystal lattice and surface-bound Sr, respectively. The chemical environment of nonlattice or surface-bound Sr could be attributed to the formation of SrO or Sr(OH)₂. As the distribution of Sr is shifted from the crystal lattice Sr concentration in LSC A to surface-bound Sr in IPL LSCs, it would be beneficial for the electron transfer and oxygen exchange pathways during ORR and OER processes.²² The Co 2p spectrum contains 2p_{3/2} and 2p_{1/2} peaks that are located at 780 ± 0.2 and 795 ± 0.2 eV, respectively, Figure 1c. The spin–orbit doublet separation (~15.1 eV) and the intensity ratio (~0.5) are characteristic of Co²⁺ and Co³⁺ ions. In the O 1s spectra, low-energy component (~528.7 eV) can be assigned to the lattice oxygen component and the high-energy

component (~530.9 eV) can be related to the perovskite lattice termination layer (529.8–531.0 eV), similar to that of Sr peaks, Figure 1d. The high-energy surface oxygen component appears to reduce with increasing temperature, in this case, with increasing IPL energy, as observed from Figure 1b,d. The distribution of oxygen appears to have shifted greatly from lattice oxygen species (528.1 eV, O²⁻) in LSC A, to electrophilic oxygen species (529.2 eV, O₂²⁻/O⁻) for IPL-sintered LSC 10, 30, and 50. That is, an obvious peak shift is observed between the conventionally sintered and IPL-sintered products from Sr 3d and O 1s peaks, while a consistently large peak width was observed from the La 3d and Co 3p peaks. The XPS survey that confirms the presence of La 3d, Sr 3d, Co 2p, and O 1s is included in Figure 1e (also refer Figure S1).^{9,23}

The X-ray diffraction patterns in Figure 1f reveal the phase composition and crystallinity of the synthesized LSC catalysts. A single perovskite phase is formed for all the LSC materials, both in IPL-treated and the conventionally sintered LSC A. The peaks appear narrow and well expressed referring to the crystallinity of the synthesized perovskites. The main characteristic peak at $2\theta = 33^\circ$ corresponds to the (104) plane of LSC. The characteristic peaks at $2\theta = 23.2, 33, 33.2, 40.7, 47.5, 53.4, 59, 69.1, 69.5, 74.2$, and 79.1° can be indexed to the *hkl* planes of (012), (110), (104), (202), (024), (122), (214), (220), (208), (312), and (128), respectively (JCPDS no. 36-1393). No other impurity peaks are detected in the patterns. The peak intensity variation among IPL-treated samples and thermally annealed sample suggests the possible structural variation due to heat treatment. The LSC A appears highly crystalline compared to IPL LSC 10, 30, and 50. The average crystallite size is calculated using the Scherrer equation with the main peak at $2\theta = 33^\circ$, to be 23.39, 24.73, and 26.23, and 34.62 nm, for samples 10, 30, 50, and A, respectively. The crystal size appears to gradually increase from LSC 10 through 50.

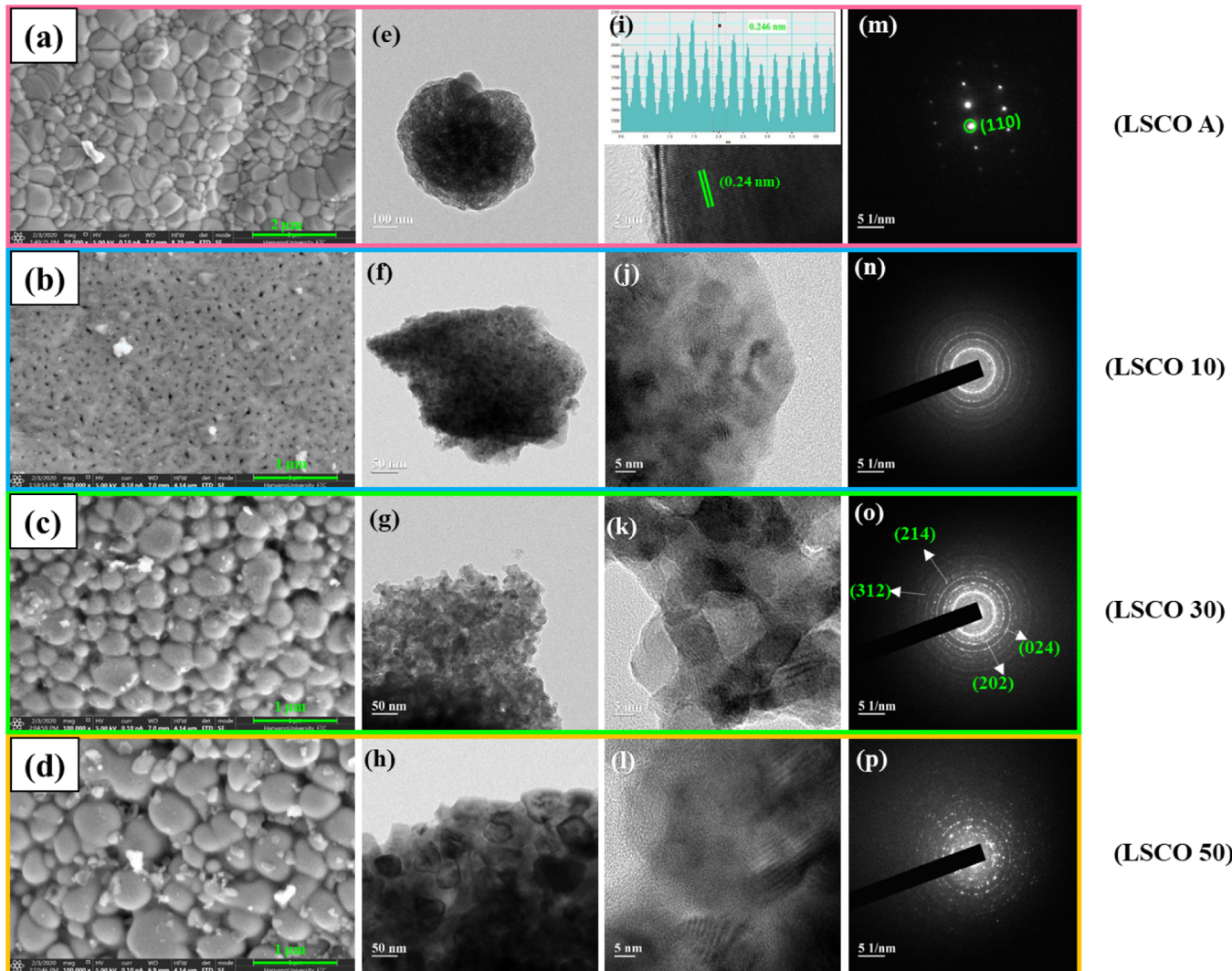


Figure 2. (a–d) FE-SEM micrographs, (e–l) HR-TEM micrographs, and (m–p) SAED pattern of the prepared LSC perovskites namely, LSC 10, 30, 50, and LSC A.

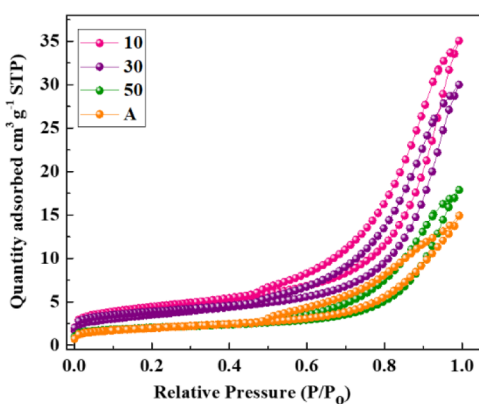


Table 1

Samples	BET Surface Area $\text{m}^2 \text{g}^{-1}$	Average Pore size Å	Total pore volume $\text{cm}^3 \text{g}^{-1}$
Pristine LSC	6.97	116.41	0.020
LSC 10	14.32	139.45	0.049
LSC 30	12.20	140.07	0.042
LSC 50	7.20	139.62	0.025
LSC A	0.73	-	-

Figure 3. N_2 adsorption/desorption isotherm of the prepared perovskite LSC; inset Table 1 summarizes the surface area and pore properties.

The SEM images show the structural characteristics and variations in thermally annealed and IPL-treated materials (Figure 2a–d). From SEM micrographs, LSC A (Figure 2a) appears to be a compact and dense nonporous surface compared to the IPL-treated materials. LSC 10 in Figure 2b shows a highly porous morphology with uniform distribution

of nanoparticles, while LSC 30 (2c) shows an increase in the particle size as well as the pore size. LSC 50 (2d), on the other hand, shows much larger particles with not so uniform distribution and some possible agglomeration. The pristine LSC before heat treatment contained assorted large size particles, which showed uniformity after sintering at 1000 °C

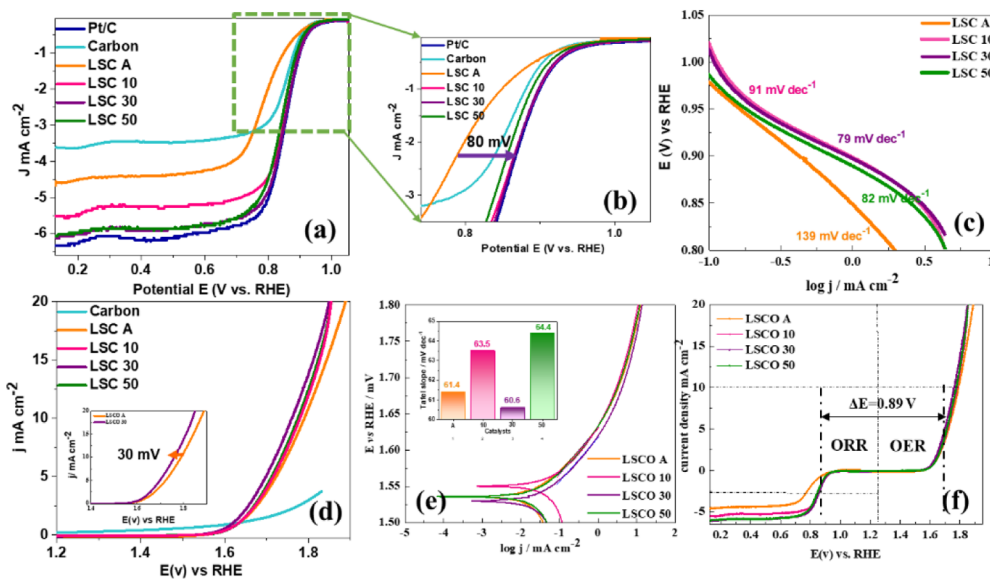


Figure 4. LSV of perovskite LSC (a) ORR, (b) magnified image of (a), (c) ORR TAFEL slopes, (d) OER, (e) OER TAFEL slopes, and (f) ORR–OER performance. Inset Table 2 summarizes the values deduced from Figure 5a and Table 3 summarizes the potential gap ΔE (V).

(LSC A), refer Supporting Information Figure S2. On the other hand, the particle size tends to increase with the increase in IPL energy as seen in Figure 2b–d. The HR-TEM images provided in Figure 2e–l detail the morphology, crystal phases, and defects of the LSC materials. The apparent increase in the particle size of IPL-treated LSC is clearly observed from HR-TEM micrographs, Figure 2j–l. The HR-TEM image and selected area electron diffraction (SAED) pattern were used to reveal the crystal superstructure, which shows the single crystalline nature of LSC A (Figure 2i,m) with a d spacing of 0.26 nm that corresponds to LSC (110) planes (JCPDS no. 36-1393), consistent with that of the XRD planes. The SAED of LSC 10, 30, and 50 shows concentric rings that imply their polycrystalline nature. Nevertheless, the poly crystallinity tends to decrease with increase in IPL energy (Figure 2m–p). The observed Debye rings are indexed to (214), (312), (024), and (202) of the rhombohedral phase of LSC, which is also compatible with the XRD planes, Figure 2o.

To understand the porosity and surface properties, BET was measured. The surface characteristics mainly surface area pore size, and volume are key factors to contribute electrochemically active redox sites and fast ion diffusion kinetics. The adsorption/desorption isotherm in Figure 3 shows type IV characteristic curves for the LSC materials declaring the presence of mesoporous solids. The hysteresis shows type 3 features that are found on solids consisting of particles forming pore slits. In detail, the as-synthesized pristine LSC has a surface area of $6.97 \text{ m}^2 \text{ g}^{-1}$, which significantly decreased to $0.73 \text{ m}^2 \text{ g}^{-1}$ for LSC A. This could be because of the Sr-rich surface of perovskite oxide formed as a result of heat treatment, as noted in XPS analysis. On the contrary, the surface area increased to 14.32 for LSC 10, 12.2 for LSC 30, and 7.2 for LSC 50. The measured surface area and pore properties are listed in Figure 3. From Figure 3, it is fascinating that IPL has a considerable effect on the pore size and volume, as well. The surface area is expected to have a positive effect on the catalytic process that takes place on the surface of the catalyst while the mass transport process inside the catalyst would be influenced

by the pore characteristics. The BET analysis further adds credibility to the crystallinity and morphology analyses.

Electrocatalytic Activity in Aqueous Media. The electrochemical behavior of the LSC catalysts is studied in 0.1 M aqueous KOH electrolyte using a RDE system by LSV. The ORRs of LSC materials were recorded in the cathodic reduction region -0.8 and 0.3 V versus Hg/HgO at a scan rate of 20 mV s^{-1} and a rotation speed of 1600 rpm, and referenced to RHE, Figure 4a. The catalytic activities are qualitatively estimated from the onset potential, half wave potential, and limiting current measured from LSV. Onset potential value is expected to be lower for ORR, in this case indicating a more positive value. The onset potentials of LSC 10, LSC 30, and LSC 50 are measured to be 0.92 , 0.92 , and 0.90 V, respectively, which are more positive than that of LSC A of 0.88 V. The half wave potential $E_{1/2}$ (V) was measured to be 0.86 , 0.87 , and 0.84 for LSC 10, LSC 30, and LSC 50, respectively, compared to 0.78 V for LSC A. The onset potential and half-wave potentials of the IPL-treated LSC and LSC A are comparable to that of the commercial Pt/C catalyst with corresponding values of 0.92 and 0.87 V, respectively, under the same experimental conditions, Figure 4a. The measured limiting currents (j) attributed to diffusion currents are measured to be -5.5 , -6.1 , and -6.0 mA cm^{-2} , for LSC 10, LSC 30, and LSC 50, respectively, compared to LSC A with -4.5 mA cm^{-2} . Overall, the IPL-treated LSC appears to outperform the conventional LSC in terms of ORR activity with a positively shifted onset potential, half-wave potential, and high limiting current. Among the IPL-treated LSC electrocatalysts, LSC 30 exhibits superior performance, where the overall ORR performance could be represented as LSC 30 > LSC 50 > LSC 10. Even so, the lowest performed LSC 10 is much better than the conventionally annealed LSC A. These results confirm the fact that IPL-sintered LSCs are orders of magnitude better than conventional LSC A. It should be noted that the ORR performance varies with applied IPL energy, that is, as the IPL energy increases from 10 to 30 J cm^{-2} , LSC 30 performs better than LSC 10. However, on further increase of energy from 30 to 50 J cm^{-2} , LSC 50 tends to decline in electrocatalytic

Table 2

Name	Onset potential E(V)	Half wave potential E _{1/2} (V)	Limiting current (mA cm ⁻²)
LSCO A	0.88	0.78	-4.5
LSCO 10	0.92	0.85	-5.5
LSCO 30	0.92	0.87	-6.1
LSCO 50	0.90	0.84	-6.0

Table 3

Name	ORR: E _{1/2} (V)	OER:E(V) at j=10 mA cm ⁻²	Oxygen electrode ΔE(V)
A	0.78	1.79	1.0
10	0.85	1.77	0.92
30	0.87	1.76	0.89
50	0.84	1.77	0.93

Table 1. Bifunctional Activity of Recently Reported Perovskites in Alkaline Media

catalyst	OER (V) @ 10 mA cm ⁻²	ORR @ $E_{1/2}$ (V)	ΔE (V)	refs (year)
mesoporous La _{0.5} Sr _{0.5} CoO _{2.91} nanowire	1.84	0.78	1.06	27 (2012)
Fe–N _x /C/LS8SCF	1.68	0.82	0.86	28 (2014)
LSC	0.87	0.89	1.08	8 (2015)
La _{0.58} Sr _{0.4} Co _{0.2} Fe _{0.8} O ₃ /N-CNT	1.639	0.81	0.83	29 (2016)
La _{0.95} FeO _{3-δ}	1.64	0.58	1.06	31 (2016)
LSC nanospheres	~1.51	~0.74	0.77	12 (2017)
LSFCO/KB	1.65	0.77	0.88	32 (2018)
30% Pd decorated LSC	1.72	0.78	0.94	34 (2019)
La _{1.5} Sr _{0.5} NiMn _{0.5} Ru _{0.5} O ₆ double perovskite	1.66	0.83	0.83	35 (2019)
nano LSCF@Pd	1.71	0.78	0.93	33 (2019)
LSC 30	1.76	0.87	0.89	this work

activity, falling behind LSC 30 but still better than LSC 10. To comprehend, the onset potential, half wave potential, and limiting current values of all the LSC catalysts measured from the ORR (Figure 4a) are summarized in Figure 4. Earlier studies have reported the improved OER activity with conventionally annealed LSC at 1000 °C.^{6,12–16,23} In this case, remarkable ORR activity better than (<80 mV) conventional LSC A is achieved.²⁴ The kinetic currents are derived from the ORR performance in Figure 4a and explained with characteristic Tafel slopes in Figure 4c. The ORR Tafel slope of LSC A is found to be 139 V dec⁻¹, while LSC 10, LSC 30, and LSC 50 show 91, 79 and 82 V dec⁻¹, respectively. LSC 30 shows a comparatively low slope value indicating less bandgap energy, which in turn would result in low overpotential. The RDE measurements were conducted at various rotating rates (400–2400 rpm) and the results show a steady increase in the limiting diffusion current with respect to the rotation speed, demonstrating excellent ORR activity for the LSC catalysts (refer Figure S3 of Supporting Information). To quantitatively evaluate the electrocatalytic activities of LSC catalysts toward ORR, the current density at a specific potential, specific activity mA cm⁻²; and, current density at a specific overpotential with respect to mass loading, mass activity A g⁻¹; are calculated and provided in Figure S4a,b. The impressive activity enhancement of IPL LSC, which is more than double that of conventional LSC A is ascribed to the unique structural modification created by IPL treatment. The high mass and specific activity values obtained for LSC 30 are indicative of its high intrinsic electrocatalytic activity, making it the most efficient ORR catalyst among all.

To characterize OER activity, the LSV polarization curve was recorded between 0.3 and 1.0 V versus Hg/HgO in the anodic region under similar conditions to those of ORR at 1600 rpm, and the values are referenced to RHE, as given in Figure 4d. The anodic peaks are observed at 1.65, 1.63, 1.64, and 1.65 V for LSC 10, 30, 50, and LSC A, respectively. The overall OER activity of LSC could be depicted as follows LSC 30 > LSC 50 > LSC 10 > LSC A, following a similar trend of ORR activity. Compared to ORR activity, there are not much improvements in the OER performance. However, a small negative shift of 30 mV is observed in the OER onset potential of IPL-treated LSC materials compared to LSC A, demonstrating better kinetics. OER Tafel slopes of 63.5, 60.6, and 64.4 mV dec⁻¹, in the lower overpotential region, are measured for LSC 10, LSC 30, and LSC 50, respectively, compared to 61.4 mV dec⁻¹ for LSC A, Figure 4e. The change in the Tafel slope values of the catalysts distinguishes their rate-determining step of OER reactions. LSC 30 has the lowest slope value as

expected, and the increase in Tafel slopes of LSC 50 and LSC 10 could be because of the reduction in the effective electrode surface area, or the mass transfer limitation. In LSC perovskite oxides, La essentially influences the oxygen adsorption capability while Sr influences the activity of as-adsorbed oxygen.^{22,23} Thus, the large size LSC A obtained by traditional high-temperature sintering exhibits poor mass transfer and limited active sites, while IPL-treated LSC especially LSC 30 portrays excellent activity toward ORR and OER owing to its unique surface modification by IPL.

To recognize and understand better, the LSV polarization curves for ORR and OER are plotted collectively in Figure 4f where the current density is normalized to the electrode area (0.196 cm²). There are no additional peaks found in ORR or OER reactions assuring a one-step reversible reaction with proper reduction and evolution of oxygen. The overpotential was calculated from the difference between OER and ORR, $\Delta(\text{OER}-\text{ORR})$ potentials as in Figure 4. The potential at $j_{\text{ORR}} = \sim E_{1/2} \text{ mA cm}^{-2}$ (V) is selected for ORR activity and OER activity was judged by the potential required to oxidize water (at $j_{\text{OER}} = 10.0 \text{ mA cm}^{-2}$).⁸ ΔE (V) is calculated to be 0.92, 0.89, and 0.93 V for LSC 10, 30, and 50, respectively, compared to that of 1.0 V of LSC A. Apparently LSC 30 has the lowest ΔE (V) = 0.89 V as expected, displaying a dominant bifunctionality over all other LSC materials. The obtained value is among the best reported values as shown in Table 1, which compares some of the LSC-based perovskite bifunctional catalysts in recent times in alkaline medium. The overpotentials (<1.0 V) of IPL-treated LSC oxygen catalysts are lower than some of the recently reported catalysts, which is favorable for application as air cathodes of metal air batteries.^{12,24–35}

The catalytic activity (ORR) of the LSC catalysts were qualitatively estimated from the reduction peak potentials of CV recorded between –0.8 and 0.3 V versus Hg/HgO at 20 mV s⁻¹ in the oxygen-saturated aqueous 0.1 M KOH electrolyte as shown in Figure S5a. The voltammograms in Figure S4a are identical except for their peak positions. A positively shifted reduction peak could be noted for all the IPL-treated LSC compared to LSC A. A similar trend of reduction potential follows here with LSC 30 showing a positive onset potential closely followed by LSC 50 and LSC 10. Interestingly, LSC 30 also shows the CV curve with a large surface area compared to others, which could be attributed to its high surface area which in turn resulted in a large electrochemically active surface, as seen in Figure 3. From Figure 3, it can be inferred that LSC 10 has a high BET surface area compared to LSC 30. However, LSC 30 has a high surface

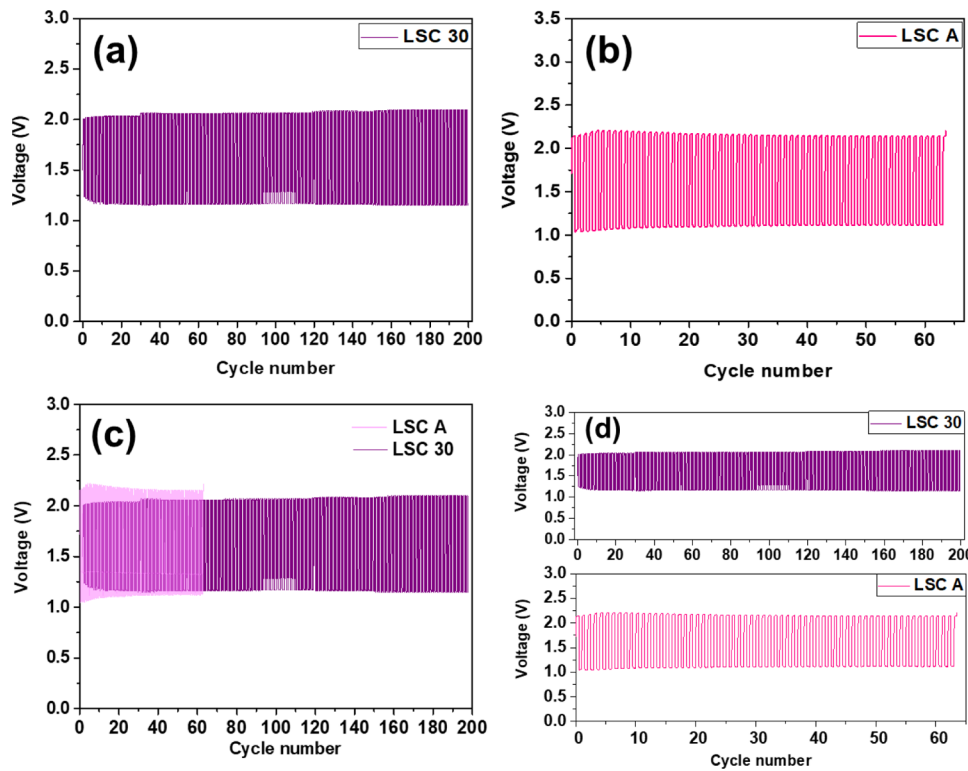


Figure 5. Zinc–air cell performance of (a) LSC 30, (b) LSC A, and (c,d) collective performance of LSC 30 and LSC A.

area, high average pore size, and pore volume compared to LSC 10. This is conclusive evidence that even though surface area does not influence the catalytic properties directly, they undoubtedly provide an increased number of active sites and promote the catalytic reactions. Furthermore, the charge area was calculated by integration of area under the cathodic reduction peak (E_{p1}), which was more than double the value for LSC 30 compared to LSC A. This also justifies the large electrochemically active surface area of LSC 30. LSC 30 if applied as the air-cathode of metal air batteries is expected to result in high capacity and low over potential.

To test this hypothesis and to find out the possible application of LSC 30 as the air cathode in metal air batteries, LSC 30 was employed in a practical zinc–air cell for cyclability. The LSC-catalyzed zinc–air cells exhibited an open circuit voltage of 1.4 V. Figure 5a shows the rechargeability of the electrode tested by galvanostatic recurrent pulse method constituting 5 min charge and 5 min discharge at a constant current density of 5 mA cm^{-2} . A stable cycle performance is seen for 200 cycles with a voltage gap of $\sim 0.9 \text{ V}$. To compare, the test cell performance of LSC A is included in Figure 5b, which shows stable performance for 64 cycles with a voltage gap of $\sim 1.1 \text{ V}$. The performances of LSC 30 and LSC A are merged in Figure 5c,d to distinguish and understand. From Figure 5c, the voltage gap seems to be greatly reduced for LSC 30-catalyzed cell compared to LSC A. From Figure 5d, a steady cycling is observed for both LSC A and LSC 30 with no modulations. IPL-sintered LSC 30 exhibits better cyclability and stability compared to conventional LSC A. However, a separate in-depth study is necessary to understand the detailed cell performance and the mechanism involved. Nevertheless, it could be suggested from the cyclability data that further modification of LSC 30, like inclusion of the OER active hybrid material on the surface

of LSC 30, could possibly improve the electrode performance and further reduce the voltage gap.

In summary, IPL treatment has tremendously reduced the synthesis process and time of LSC materials and rejuvenated a class of highly electrocatalytically active LSC. Among the IPL-treated LSCs, LSC 30 shows comparatively faster kinetics for ORR and OER with positively shifted onset potential for ORR, a high limiting current, negatively shifted OER onset potential, and a lower over potential, Figures 4, 5, and S5. As the IPL energy increased, the catalytic performance of LSC clearly varies, Figure 4. From Figure 3, IPL-treated LSCs exhibit remarkable surface properties with high porosity. Apart from aiding high porosity that facilitates the electron transfer and abundant oxygen flow, IPL treatment creates crystal defects that played an important role in the electrochemical characteristics. The oxygen vacancies in the crystal structures of the materials have promoted the charge transfer kinetics resulting in improved catalytic activities simultaneously for both oxygen reactions.^{24,25} That is, during the ORR electrocatalysis, there is a dynamic reduction of molecular oxygen and a subsequent addition into solid-state O^{2-} , and vice versa. These oxygen vacancies behave as donors or acceptors, augmenting the charge transfer between the adsorbent and the adsorbate. Subsequently, in oxygen-deficient oxides, there is a simultaneous filling and creation of lattice oxygen vacancies, which plays a predominant role in determining their intrinsic ORR/OER activities.^{36–39} IPL has influenced the surface characteristics, which significantly changes its morphology, as in Figure 2. From the XRD and SAED patterns in Figures 1 and 2, respectively, LSC A exhibits a highly crystalline structure, which has considerably changed for IPL-treated LSC with an increase in the crystal size as well as polycrystallinity. The highly crystalline LSC A is less reactive to ORR. Notable performance of LSC 30 could also be seen as a result of better

electronic movement that facilitates OH^- transportation to its active sites. The superior performance of LSC 30 among the IPL-treated LSCs is mainly attributed to the surface characteristics and morphology of the material. LSC 30 shows an increase in the particle size as well as pore size as observed from FE-SEM images in Figure 2a–d. While LSC 10 and 50 also possess a porous surface, the average pore size is comparatively large for LSC 30 (Figure 3). The high porosity is directly associated with the better electron transfer and abundant oxygen flow. XPS confirms the distribution of oxygen to have transferred from lattice oxygen species (528.1 eV, O^{2-}) in LSC A, to electrophilic oxygen species (529.2 eV, $\text{O}_2^{2-}/\text{O}^-$) for IPL-treated LSC 10, LSC 30, and LSC 50. This is the main reason for the improved OER kinetics. The OH^- peak inclination from LSC A to IPL-treated LSC ensures the acceleration of catalytic reaction. As a result, IPL-sintered LSCs deliver orders of magnitude better activity for ORR and OER. When applied in zinc–air batteries, LSC 30 delivered a stable cycling performance for 200 cycles. The development of perovskites deserves more efforts and from the overall performance and results of this study, it could be confirmed that IPL is a promising clean energy technology unfolding immense possibilities for rapid and easy fabrication of perovskites with desirable properties.

CONCLUSIONS

A simple and ultrafast technique to synthesize as well as enhance the electrocatalytic activity of perovskite LSCs for oxygen catalysis has been demonstrated in this work. The LSC particles were prepared using the IPL sintering technique accomplished in milliseconds by high-energy flashes that outperformed the conventionally sintered LSC both by time and performance. The as-synthesized LSC possessed desirable physical properties such as a high surface area and porosity. Their catalytic activities were significantly improved, surpassing the catalytic performance of conventionally annealed LSC A. 30 J cm^{-1} was found to be the optimum IPL energy for sintering LSC with its dominant overall performance as a bifunctional catalyst. When applied as an air cathode, LSC 30 delivered a steady cycling performance for 200 cycles with a low voltage gap. This study simplified the agile synthesis of highly active electrocatalysts for air-cathode applications.

ASSOCIATED CONTENT

Supporting Information

The Supporting Information is available free of charge at <https://pubs.acs.org/doi/10.1021/acs.energyfuels.0c03147>.

Irradiation energy, time, and pulse duration details of IPL sintering at different energy density; deconvolution peaks of LSC obtained from XPS analysis; FESEM micrographs; measured ORR–LSV curves of IPL-treated LSCs at different rpm; specific activity chart and mass activity chart; and cyclic voltammogram of the IPL-treated LSC materials and LSC A ([PDF](#))

AUTHOR INFORMATION

Corresponding Author

Young-Beom Kim — Department of Mechanical Convergence Engineering, Hanyang University, Seoul 04763, Republic of Korea;  orcid.org/0000-0002-0307-0595
Email: ybkim@hanyang.ac.kr

Authors

Maria Christy — Department of Mechanical Convergence Engineering and Department of Chemical Engineering, Hanyang University, Seoul 04763, Republic of Korea;  orcid.org/0000-0002-6769-9237

Hashikaa Rajan — Department of Chemical Engineering, Hanyang University, Seoul 04763, Republic of Korea

Hwicheul Yang — Department of Mechanical Convergence Engineering, Hanyang University, Seoul 04763, Republic of Korea;  orcid.org/0000-0002-6974-8696

Complete contact information is available at:
<https://pubs.acs.org/10.1021/acs.energyfuels.0c03147>

Notes

The authors declare no competing financial interest.

ACKNOWLEDGMENTS

M.C. and Y.-B.K. gratefully acknowledge financial support from the program for fostering next-generation researchers in engineering of National Research Foundation of Korea (NRF) funded by the Ministry of Science, ICT, and Future Planning (no. 2017H1D8A2032495).

REFERENCES

- (1) Zhu, J.; Li, H.; Zhong, L.; Xiao, P.; Xu, X.; Yang, X.; Zhao, Z.; Li, J. Perovskite Oxides: Preparation, Characterizations, and Applications in Heterogeneous Catalysis. *ACS Catal.* **2014**, *4*, 2917–2940.
- (2) Ciambelli, P.; Cimino, S.; Lisi, L.; Faticanti, M.; Minelli, G.; Pettiti, I.; Porta, P. La, Ca and Fe oxide perovskites: preparation, characterization and catalytic properties for methane combustion. *Appl. Catal., B* **2001**, *33*, 193–203.
- (3) Chen, D.; Wang, J.; Zhang, Z.; Shao, Z.; Ciucci, F. Boosting oxygen reduction/evolution reaction activities with layered perovskite catalysts. *Chem. Commun.* **2016**, *52*, 10739–10742.
- (4) Arandiyani, H.; Wang, Y.; Sun, H.; Rezaei, M.; Dai, H. Ordered meso- and macroporous perovskite oxide catalysts for emerging applications. *Chem. Commun.* **2018**, *54*, 6484–6502.
- (5) Zhao, Y.; Liu, T.; Shi, Q.; Yang, Q.; Li, C.; Zhang, D.; Zhang, C. Perovskite oxides $\text{La}_0.4\text{Sr}_0.6\text{Co}_{1-x}\text{Mn}_1\text{xO}_3$ ($x = 0, 0.2, 0.4$) as an effective electrocatalyst for lithium–air batteries. *Green Energy Environ.* **2018**, *3*, 78–85.
- (6) Lee, J. J.; Oh, M. Y.; Nahm, K. S. Effect of ball milling on electrocatalytic activity of perovskite $\text{La}_{0.6}\text{Sr}_{0.4}\text{CoO}_{3-\delta}$ applied for lithium air battery. *J. Electrochim. Soc.* **2016**, *163*, A244–A250.
- (7) Januschewsky, J.; Ahrens, M.; Opitz, A.; Kubel, F.; Fleig, J. Optimized $\text{La}_{0.6}\text{Sr}_{0.4}\text{CoO}_{3-\delta}$ thin-film electrodes with extremely fast oxygen-reduction kinetics. *Adv. Funct. Mater.* **2009**, *19*, 3151–3156.
- (8) Oh, M. Y.; Jeon, J. S.; Lee, J. J.; Kim, P.; Nahm, K. S. The bifunctional electrocatalytic activity of perovskite $\text{La}_{0.6}\text{Sr}_{0.4}\text{CoO}_{3-\delta}$ for oxygen reduction and evolution reactions. *RSC Adv.* **2015**, *5*, 19190–19198.
- (9) Van der Heide, P. A. W. Systematic X-ray photoelectron spectroscopic study of $\text{La}_{1-x}\text{Sr}_x$ -based perovskite-type oxides. *Surf. Interface Anal.* **2002**, *33*, 414–425.
- (10) Konysheva, E. Y.; Francis, S. M.; Irvine, J. T. S.; Rolle, A.; Vannier, R.-N. Red–ox behaviour in the $\text{La}_{0.6}\text{Sr}_{0.4}\text{CoO}_3\text{CeO}_2$ system. *J. Mater. Chem.* **2011**, *21*, 15511–15520.
- (11) Pechini, M. P. U.S. Patent 3,330,697, 1967.
- (12) Sennu, P.; Aravindan, V.; Nahm, K. S.; Lee, Y.-S. Exceptional catalytic activity of hollow structured $\text{La}_{0.6}\text{Sr}_{0.4}\text{CoO}_{3-\delta}$ perovskite spheres in aqueous media and aprotic Li– O_2 batteries. *J. Mater. Chem. A* **2017**, *5*, 18029–18037.
- (13) Lin, Q.; Zhu, Y.; Hu, Z.; Yin, Y.; Lin, H.-J.; Chen, C.-T.; Zhang, X.; Shao, Z.; Wang, H. Boosting the oxygen evolution catalytic performance of perovskites via optimizing calcination temperature. *J. Mater. Chem. A* **2020**, *8*, 6480–6486.

- (14) Zhu, Y.; Tahini, H. A.; Hu, Z.; Chen, Z. G.; Zhou, W.; Komarek, A. C.; Lin, Q.; Lin, H. J.; Chen, C. T.; Zhong, Y.; Fernández-Díaz, M. T.; Smith, S. C.; Wang, H.; Liu, M.; Shao, Z. Boosting Oxygen Evolution Reaction by Creating Both Metal Ion and Lattice-Oxygen Active Sites in a Complex Oxide. *Adv. Mater.* **2020**, *32*, 1905025.
- (15) Zhu, Y.; Lin, Q.; Zhong, Y.; Tahini, H. A.; Shao, Z.; Wang, H. Metal oxide-based materials as an emerging family of hydrogen evolution electrocatalysts. *Energy Environ. Sci.* **2020**, *13*, 3361–3392.
- (16) Zhu, Y.; Lin, Q.; Hu, Z.; Chen, Y.; Yin, Y.; Tahini, H. A.; Lin, H. J.; Chen, C. T.; Zhang, X.; Shao, Z.; Wang, H. Self-assembled Ruddlesden-Popper/Perovskite hybrid with lattice-oxygen activation as a superior oxygen evolution electrocatalyst. *Small* **2020**, *16*, 2001204.
- (17) Jang, K.; Yu, S.; Park, S.-H.; Kim, H.-S.; Ahn, H. Intense pulsed light-assisted facile and agile fabrication of cobalt oxide/nickel cobaltite nanoflakes on nickel-foam for high performance supercapacitor applications. *J. Alloys Compd.* **2015**, *618*, 227–232.
- (18) Zhong, Z.; Lee, H.; Kang, D.; Kwon, S.; Choi, Y.-M.; Kim, I.; Kim, K.-Y.; Lee, Y.; Woo, K.; Moon, J. Continuous patterning of copper nanowire-based transparent conducting electrodes for use in flexible electronic applications. *ACS Nano* **2016**, *10*, 7847–7854.
- (19) Dexter, M.; Gao, Z.; Bansal, S.; Chang, C. H.; Malhotra, R. Temperature, crystalline phase and influence of substrate properties in intense pulsed light sintering of copper sulfide nanoparticle thin films. *Sci. Rep.* **2018**, *8*, 2201.
- (20) Park, J.-S.; Chung, W.-H.; Kim, H.-S.; Kim, Y.-B. Rapid fabrication of chemical-solution-deposited La_{0.6}Sr_{0.4}CoO_{3-δ} thin films via flashlight sintering. *J. Alloys Compd.* **2017**, *696*, 102–108.
- (21) Tsvetkov, N.; Lu, Q.; Sun, L.; Crumlin, E. J.; Yildiz, B. Improved chemical and electrochemical stability of perovskite oxides with less reducible cations at the surface. *Nat. Mater.* **2016**, *15*, 1010–1016.
- (22) Crumlin, E. J.; Mutoro, E.; Liu, Z.; Grass, M. E.; Biegalski, M. D.; Lee, Y.-L.; Morgan, D.; Christen, H. M.; Bluhm, H.; Shao-Horn, Y. Surface strontium enrichment on highly active perovskites for oxygen electrocatalysis in solid oxide fuel cells. *Energy Environ. Sci.* **2012**, *5*, 6081–6088.
- (23) She, S.; Zhu, Y.; Chen, Y.; Lu, Q.; Zhou, W.; Shao, Z. Realizing ultrafast oxygen evolution by introducing proton acceptor into perovskites. *Adv. Energy Mater.* **2019**, *9*, 1900429.
- (24) Hardin, W. G.; Slanac, D. A.; Wang, X.; Dai, S.; Johnston, K. P.; Stevenson, K. J. Highly active, nonprecious metal perovskite electrocatalysts for bifunctional metal–air battery electrodes. *J. Phys. Chem. Lett.* **2013**, *4*, 1254–1259.
- (25) Hong, W. T.; Risch, M.; Stoerzinger, K. A.; Grimaud, A.; Suntivich, J.; Shao-Horn, Y. Toward the rational design of non-precious transition metal oxides for oxygen electrocatalysis. *Energy Environ. Sci.* **2015**, *8*, 1404–1427.
- (26) Christy, M.; Arul, A.; Kim, Y. B. Carbide composite nanowire as bifunctional electrocatalyst for lithium oxygen batteries. *Electrochim. Acta* **2019**, *300*, 186–192.
- (27) Zhao, Y.; Xu, L.; Mai, L.; Han, C.; An, Q.; Xu, X.; Liu, X.; Zhang, Q. Hierarchical mesoporous perovskite La_{0.5}Sr_{0.5}CoO_{2.91} nanowires with ultrahigh capacity for Li-air batteries. *Proc. Natl. Acad. Sci. U.S.A.* **2012**, *109*, 19569–19574.
- (28) Rincón, R. A.; Masa, J.; Mehrpour, S.; Tietz, F.; Schuhmann, W. Activation of oxygen evolving perovskites for oxygen reduction by functionalization with Fe–Nx/C groups. *Chem. Commun.* **2014**, *50*, 14760–14762.
- (29) Elumeeva, K.; Masa, J.; Tietz, F.; Yang, F.; Xia, W.; Muhler, M.; Schuhmann, W. A simple approach towards high-performance perovskite-based bifunctional oxygen electrocatalysts. *ChemElectroChem* **2016**, *3*, 138–143.
- (30) Park, H. W.; Lee, D. U.; Zamani, P.; Seo, M. H.; Nazar, L. F.; Chen, Z. Electrospun porous nanorod perovskite oxide/nitrogen doped graphene composite as a bi-functional catalyst for metal air batteries. *Nano Energy* **2014**, *10*, 192–200.
- (31) Zhu, Y.; Zhou, W.; Yu, J.; Chen, Y.; Liu, M.; Shao, Z. Enhancing electrocatalytic activity of perovskite oxides by tuning cation deficiency for oxygen reduction and evolution reactions. *Chem. Mater.* **2016**, *28*, 1691–1697.
- (32) Alegre, C.; Modica, E.; Aricò, A. S.; Baglio, V. Bifunctional oxygen electrode based on a perovskite/carbon composite for electrochemical devices. *J. Electroanal. Chem.* **2018**, *808*, 412–419.
- (33) Oh, M. Y.; Kim, J. H.; Lee, Y. W.; Kim, K. J.; Shin, H. R.; Park, H.; Lee, K. T.; Kang, K.; Shin, T. H. Enhancing bifunctional catalytic activity via a nanostructured La(Sr)Fe(Co)O_{3-δ}@Pd matrix as an efficient electrocatalyst for Li–O₂ Batteries. *ACS Appl. Energy Mater.* **2019**, *2*, 8633–8640.
- (34) Oh, M. Y.; Lee, J. J.; Park, H. S.; Kim, T.-Y.; Lee, Y.-S.; Vanchiappan, A.; Nahm, K. S. Efficient bifunctional catalytic activity of nanoscopic Pd-decorated La_{0.6}Sr_{0.4}CoO_{3-δ} perovskite toward Li–O₂ battery, oxygen reduction, and oxygen evolution reactions. *J. Ind. Eng. Chem.* **2019**, *80*, 686–695.
- (35) Retuerto, M.; Calle-Vallejo, F.; Pascual, L.; Lumbeeck, G.; Fernandez-Díaz, M. T.; Croft, M.; Gopalakrishnan, J.; Peña, M. A.; Hadermann, J.; Greenblatt, M.; Rojas, S. La_{1.5}Sr_{0.5}NiMn_{0.5}Ru_{0.5}O₆ double perovskite with enhanced ORR/OER bifunctional catalytic activity. *ACS Appl. Mater. Interfaces* **2019**, *11*, 21454–21464.
- (36) Gupta, S.; Kellogg, W.; Xu, H.; Liu, X.; Cho, J.; Wu, G. Bifunctional perovskite oxide catalysts for oxygen reduction and evolution in alkaline media. *Chem.—Asian J.* **2016**, *11*, 10–21.
- (37) Jung, J.-I.; Jeong, H. Y.; Lee, J.-S.; Kim, M. G.; Cho, J. A bifunctional perovskite catalyst for oxygen reduction and evolution. *Angew. Chem., Int. Ed.* **2014**, *53*, 4582–4586.
- (38) Jin, X.; Park, M.; Shin, S. J.; Jo, Y.; Kim, M. G.; Kim, H.; Kang, Y. M.; Hwang, S. J. Synergistic control of structural disorder and surface bonding nature to optimize the functionality of manganese oxide as an electrocatalyst and a cathode for Li–O₂ Batteries. *Small* **2020**, *16*, 1903265.
- (39) Liu, G.; Chen, H.; Xia, L.; Wang, S.; Ding, L.-X.; Li, D.; Xiao, K.; Dai, S.; Wang, H. Hierarchical mesoporous/macroporous perovskite La_{0.5}Sr_{0.5}CoO_{3-x} nanotubes: A bifunctional catalyst with enhanced activity and cycle stability for rechargeable lithium oxygen batteries. *ACS Appl. Mater. Interfaces* **2015**, *7*, 22478–22486.